

# Dense 3D Face Correspondence

Syed Zulqarnain Gilani, Faisal Shafait and Ajmal Mian

*School of Computer Science and Software Engineering, The University of Western Australia, 35 Stirling Highway, Crawley, Western Australia, 6009*

---

## Abstract

We present an algorithm that automatically establishes dense correspondences between a large number of 3D faces. Starting from automatically detected sparse correspondences on the convex hull of 3D faces, the algorithm triangulates existing correspondences and expands them iteratively along the triangle edges. New correspondences are established by matching keypoints on the geodesic patches along the triangle edges and the process is repeated. After exhausting keypoint matches, further correspondences are established by evolving level set geodesic curves from the centroids of large triangles. A deformable model (K3DM) is constructed from the dense corresponded faces and an algorithm is proposed for morphing the K3DM to fit unseen faces. This algorithm iterates between rigid alignment of an unseen face followed by regularized morphing of the deformable model. We have extensively evaluated the proposed algorithms on synthetic data and real 3D faces from the FRGCv2 and BU3DFE databases using quantitative and qualitative benchmarks. Our algorithm achieved dense correspondences with a mean localization error of 1.28mm on synthetic faces and detected 18 anthropometric landmarks on unseen real faces from the FRGCv2 database with 3mm precision. Furthermore, our deformable model fitting algorithm achieved 99.8% gender classification and 98.3% face recognition accuracy on the FRGCv2 database.

*Keywords:* Dense correspondence, 3D face, morphing, keypoint detection, level sets, geodesic curves, deformable model.

---

## 1. Introduction

Establishing dense correspondences between 3D faces is a challenging problem due to the diversity in faces. Dense correspondence is a pre-requisite for many computer vision, computer graphics and medical image analysis applications. Generating accurate 3D morphable face models is possible only after dense correspondences are established between a large number of 3D faces. Once a morphable model is available, it can be used for information transfer between the training and a test face or between two test faces by morphing the 3D model to fit the test face(s). For example, given the location of anthropometric landmarks [1] on the 3D morphable model, these landmarks can be automatically localized on unseen test faces [2]. Besides, dense correspondences and morphable models can be used for 3D face recognition [3]. Other applications include facial morphometric measurements such as asymmetry for

---

*Email address:* {zulqarnain.gilani, faisal.shafait, ajmal.mian}@uwa.edu.au (Syed Zulqarnain Gilani, Faisal Shafait and Ajmal Mian)

syndrome diagnosis [4, 5], statistical shape modelling [6, 7, 8], shape interpolation [9], non-rigid shape registration [10, 11, 12], deformation analysis [13] and recognition [14, 15, 16].

While it is possible to manually annotate a small number ( $\sim 30$ ) of correspondences for a few 3D faces, it is not feasible to manually identify dense correspondences ( $\sim 6,000$ ) between hundreds of 3D faces. Automatically establishing dense correspondences between the 3D faces of two different persons is an extremely challenging task because the facial shape varies significantly amongst individuals depending on their identity, gender, ethnicity and age [1]. The problem of dense 3D point-to-point correspondences can be formulated as follows. Given a set of  $N$  3D faces,  $\mathbf{F}_j = [x_p, y_p, z_p]^T, j = 1, \dots, N, p = 1, \dots, P_j$ , the aim is to establish a dense bijective mapping  $f : \mathbf{F}_i \rightarrow \mathbf{F}_j (i \neq j)$  over  $k$  vertices where  $1 \ll k < \min(P_i, P_j)$ . More specifically,  $(\exists p \in \mathbf{F}_i)[\exists q \in \mathbf{F}_j \parallel \mathbf{F}_i \rightarrow \mathbf{F}_j](i \neq j)$  where  $p$  and  $q$  are corresponding points on the 3D manifold  $\mathbf{F}_i$  and  $\mathbf{F}_j$  respectively. Correspondences should cover all regions of the face for high fidelity and should follow the same triangulation for shape consistency.

Existing 3D dense correspondence techniques can be grouped into descriptor based and model based techniques [17]. Descriptor based techniques match local 3D point signatures derived from the curvatures, shape index and normals. Model based approaches train a morphable model using a sparse set of correspondences and then extend them to dense correspondences. One of the earliest works for establishing dense correspondence in the descriptor based category was proposed by Wang et al. [18]. In the first step, a sparse set of corresponding points are found on the 3D human brain by minimizing the product of the Euclidean distance, surface normals and the principle curvatures calculated at these points. In the second step, correspondences are propagated by taking the middle point of the shortest path geodesic curve between each corresponding pair of points, triangulating them and repeating the procedure until dense correspondences are obtained. Sun and Abidi [19, 20] projected geodesic contours around a 3D facial point onto their tangential plane and used them as features to match two surfaces. The contours are called Finger Prints of the 3D point. This method is highly sensitive to surface noise and sampling density [21] of the underlying geometry [22]. The approach, with minor modifications, was employed by Salazar et al. [23] to establish point correspondence on 3D faces.

In the model based category, employing a Point Distribution Model coupled with 3D point signature detection approach, Nair and Cavallaro [2] estimated the location of 49 corresponding landmarks on faces. The proposed algorithm was tested on 2,350 faces of the BU3DFE [24] database. Although the method works well in the presence of noisy data, the mean error in the localization of landmarks was rather high. Lu and Jain [25] presented a multimodal approach for facial feature extraction. Using a face landmark model, the authors detected seven corresponding points on 3D faces using shape index from range images and cornerness from intensity images. Segundo et al. [26] used a curve analysis approach for landmark detection in 3D faces of the FRGCv2[27] and BU3DFE databases. They extracted features from the mean and Gaussian curvatures for detecting five facial landmarks in the nose and eye (high curvature) regions. These algorithms establish correspondences between a very sparse set of anthropometric landmarks.

Creusot et al.[28] presented a machine learning approach to detect 14 corresponding landmarks in

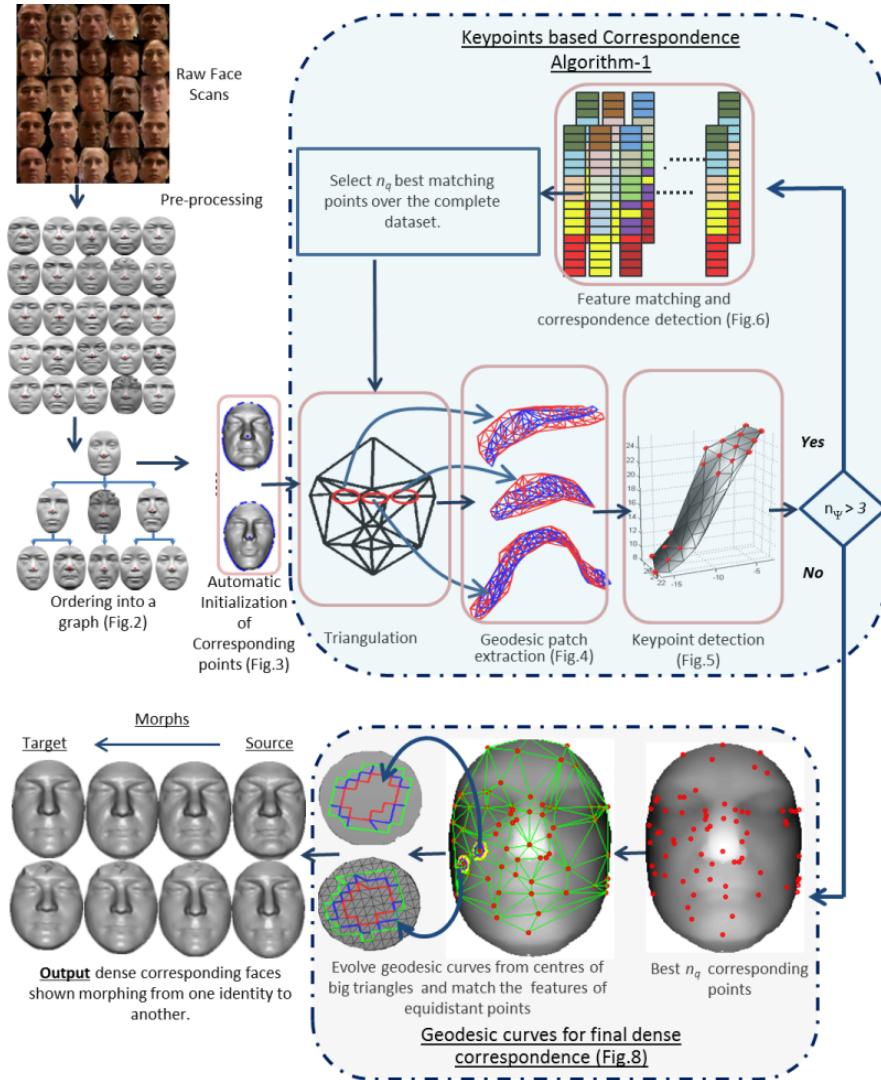


Figure 1: Block diagram of the presented dense 3D face correspondence algorithm.

3D faces. They trained an off-line LDA classifier on a set of 200 faces and a landmark model using a myriad of local descriptors. Each landmark detection is then reduced to a two class classification problem and the final result is fused. The method works well for neutral expression faces of the FRGCv2 and Bosphorus databases. Perakis et al. [29] proposed a method to detect landmarks under large pose variations using a statistical Facial Landmark Model (FLM) for the full face and another two FLMs for each side of the face. A combination of Shape Index and Spin Images is used to find key points on the face. Corresponding points are determined on the basis of minimum combined normalized Procrustes and Spin Image similarity distance from all three FLMs. This method was used to detect eight correspondences in the FRGCv2 database.

Blanz and Vetter [30] proposed a dense correspondence algorithm using optical flow on the texture and the 3D cylindrical coordinates of the face points assuming that the faces are spatially aligned. They constructed a 3D morphable face model from 100 male and female faces each. An arbitrary face was chosen as a reference and the remaining scans were registered to it by iterating between optical flow based correspondence and morphable model fitting. One potential pitfall of the texture based dense correspondence [30] is that facial texture is not always consistent with the underlying 3D facial morphology

e.g. the shape and location of eyebrows. Moreover, this algorithm requires seven manually annotated facial landmarks for initialization. Later, in [3, 31] the authors used the 3D morphable model for face recognition. Experiments were performed on only 150 pairs of 3D faces [31] from FRGCv2 database, although the total number of scans in the database are 4,007.

Passalis et al. [32] proposed an Annotated Face Model (AFM) based on an average facial 3D mesh. The model was created by manually annotating a sparse set of anthropometric landmarks [1] on 3D face scans and then segmenting it into different annotated areas. Later, Kakadiaris et al. [33] proposed elastic registration using this AFM by shifting the manually annotated facial points according to elastic constraints to match the corresponding points of 3D target models in the gallery. Face recognition was performed by comparing the wavelet coefficients of the deformed images obtained from morphing.

Based on our literature survey, existing dense correspondence techniques have one or more of the following limitations: (1) They need manually annotated landmarks on 3D faces for initialization. (2) They use texture matching to find 3D shape correspondence. (3) They correspond all faces to a single reference face neglecting the global proximity of the 3D faces. (4) They have not been tested on *complete* benchmark databases such as the FRGCv2 for face recognition, gender classification and landmark identification. (5) They have no explicit mechanism of updating the dense correspondence model.

In this context, we propose a fully automatic algorithm for establishing dense correspondences simultaneously between a large number of 3D faces. Our algorithm does not require any manual intervention and relies solely on 3D shape matching to encode accurate facial morphology. We organize the 3D faces into a minimum spanning tree based on bending energy required to deform one shape into the other so that correspondences can be propagated in a reliable way. We propose a mechanism for automatic initialization of a sparse set of correspondences on the convex hull of the 3D faces. By triangulating existing correspondences and expanding them iteratively along the geodesic patches associated with the triangle edges, new correspondences are established through keypoint descriptor matching. After exhausting keypoint matches, further correspondences are established by evolving level set geodesic curves from the centroids of large triangles. The outcome of our algorithm is a Keypoints based 3D Deformable Model (K3DM).

Our second major contribution is a deformable model fitting algorithm where K3DM is used to morph into unseen query faces. Starting from the mean face, the fitting algorithm iterates between two steps. The query face is transformed rigidly to align with the model and the model is deformed using regularized least squares to fit the query face. This algorithm converges in a few iterations and is robust to noise, outlier points, missing points, pose and expression variations.

Our final contribution is an algorithm for augmenting the K3DM. Given the K3DM and a new batch of  $M$  faces, we construct a minimum spanning tree using the nearest face to the K3DM as the root node. The K3DM is augmented by adding one face at a time, starting with the root node, and each time updating the model and deforming the updated model to better fit the next face in the spanning tree.

Evaluating dense correspondence techniques is challenging due to the inherent difficulty of obtaining ground-truth data. In the existing literature, evaluations have mostly been performed on a sparse set of anthropometric facial landmarks [29, 28] since these can be manually labelled. However, evaluation on

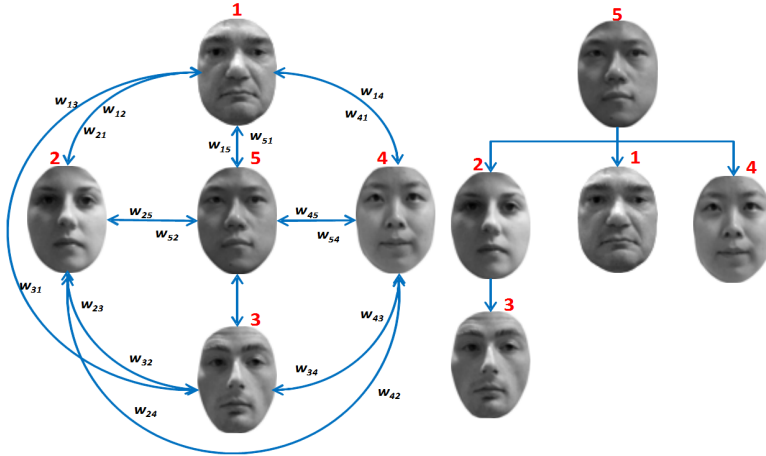


Figure 2: The directed graph  $G = (V_g, E_g)$  (Left) and the MST  $\Pi = (V_t, E_t)$  (Right) constructed from five example images of FRGCv2.

only a few ( $\leq 20$ ) anthropometric points does not show how well dense correspondences generalize to the whole face. Thus, subjective evaluations are frequently performed [30] by visually inspecting the quality of morphing between faces [34, 20]. In this paper, we show how synthetic 3D faces (Facegen<sup>TM</sup> Modeller) can be used to quantitatively evaluate dense correspondences on a large set of points ( $\geq 1,000$ ). Using the presented deformable face model, we perform extensive experiments for landmark localization (Sec. 5.1), gender classification (Sec. 5.2) and face recognition (Sec. 5.3) using real faces from the FRGCv2 [27] and BU3DFE [24] databases. Results show that our algorithm outperforms state-of-the-art application-specific algorithms in each of these areas.

## 2. Dense 3D Face Correspondence

Block diagram of our proposed dense correspondence algorithm is shown in Figure 1. Individual components are explained below and elaborated in the subsequent figures.

### 2.1. Preprocessing

The nose tip of a 3D face is detected automatically following Mian et al. [35]. Centring a sphere at the nose tip, the face is cropped. The pose of the 3D face is iteratively corrected to a canonical form using the Hotelling transform [36]. Next, holes are filled and noise is removed using the gridfit algorithm [37].

### 2.2. Organizing Faces into a Graph

Our proposed method finds corresponding points between pairs of 3D faces using features extracted at keypoints. A naive approach would be to use a single face as reference and find its correspondences to others in the dataset. However, this approach essentially ignores the proximity between the face instances and the global information underlying the population. Following Munsell et al. [38], we address this issue by pre-organizing the faces using a minimum spanning tree. Let  $G = (V_g, E_g)$  be a directed graph where each node  $V_g$  is a 3D face  $\mathbf{F}$  from the training set and each edge  $E_g$  connects two nodes  $(v_i, v_j)$  in the graph. Let the edges of the graph be weighted by  $w$ :

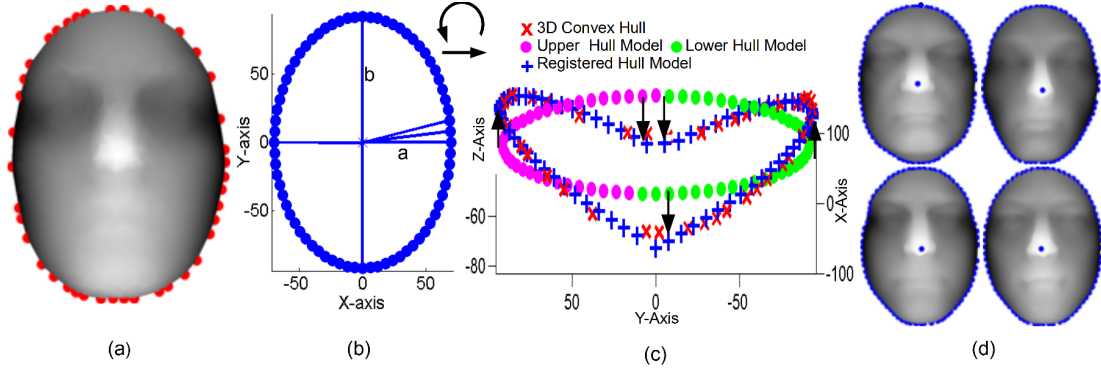


Figure 3: Initial sparse correspondence model  $\mathbf{L}$  projected on four identities of the BU3DFE dataset.

$$w(v_i, v_j) = \frac{\beta_{ij} + \beta_{ji}}{2}, \quad (1)$$

where  $\beta_{ij}$  is the amount of bending energy required to deform face  $F_i$  to  $F_j$  and is measured using the 2D thin-plate spline model [39]. Note that  $\beta_{ij} \neq \beta_{ji}$  and  $\beta_{ii} = 0$ . Using  $G$ , we construct a minimum spanning tree  $\Pi = (V_t, E_t)$  using Kruskal’s algorithm, where  $\Pi$  is a connected, acyclic and undirected graph. The node with the maximum number of children is taken as the root node.

### 2.3. Sparse Correspondence Initialization

The dense correspondence algorithm is initialized with a sparse set of automatically detected correspondences between the 3D faces. We find the points on the convex hull (shown in red in Figure 3(a)) of each sub-sampled 3D face using Barber’s algorithm [40]. Note that sub-sampling is done only for this step and the full point cloud is used for the subsequent steps. Next, we centre the face at the nose tip and form a 3D Hull Model  $\Theta$  (Figure 3(b)) given by,

$$\Theta_i = [a \cos(\theta_i), b \sin(\theta_i), 0]^T \quad (2)$$

where  $a$  and  $b$  are the measurements of horizontal and vertical extremities of the 3D face from the nose tip and  $\theta_i$  is an angle from 0 to  $2\pi$  at regular intervals of  $\delta = \pi/36$ .

The Hull Model  $\Theta$  is then registered to the convex hull points of the 3D face. The 3D hull of the face is symmetric across the horizontal axis and lies on two intersecting horizontal planes. Since, the Hull Model  $\Theta$  lies on a single horizontal plane, it is not possible to register it rigidly with the points on 3D hull. For this reason, we divide the Hull Model  $\Theta$  into two parts along the horizontal axis. These two parts are shown in a rotated view in magenta and green colours in Figure 3(c). Registration by parts seamlessly registers  $\Theta$  to the 3D convex hull as shown in blue in the figure. Registering a dense Hull Model to the 3D hull points will result in multiple duplicate correspondences because the 3D hull points of the sub-sampled mesh are sparse. To mitigate this problem, we establish correspondences using the Nearest Neighbour criterion between the Hull Model  $\Theta$  and the dense point cloud of the 3D face giving us initial corresponding points on the convex hull of each face. This process is repeated on all 3D faces in the training set resulting in a correspondence model set  $\mathbf{L} = \{\iota_1, \dots, \iota_N\}$  where  $\iota_n = [x_k, y_k, z_k]^T$ , and  $k = 1, \dots, \frac{2\pi}{\delta}$ . Some points in  $\mathbf{L}$  may still have a duplicate correspondence with their respective 3D face because of using the Nearest Neighbour (NN) method for correspondence.

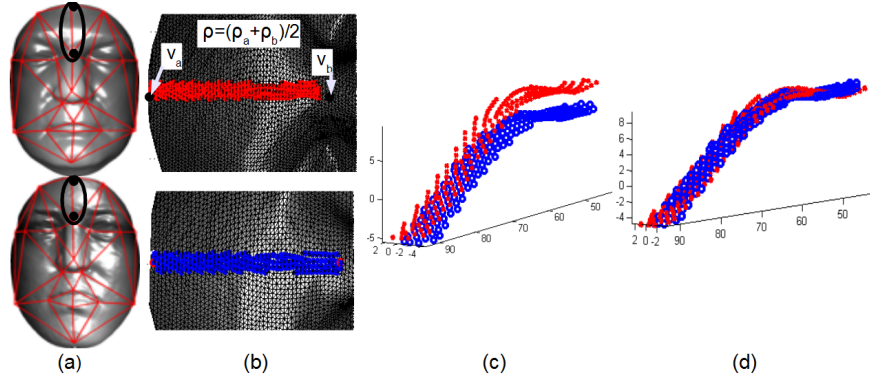


Figure 4: Illustration of geodesic patch extraction. (a) Two 3D faces with triangulation over a few corresponding points. (b) Geodesic surface patch extraction between two sample points on the forehead after rigid rotation. (c) Pointclouds of the geodesic surface patches before registration and (d) after registration.

All such duplicate correspondences are removed from  $\mathbf{L}$ . As shown in Figure 3(d), the resultant points are in good correspondence with each other across the training dataset.

#### 2.4. Triangulation and Geodesic Patch Extraction

The algorithm is initialized with the sparse correspondence model  $\mathbf{L}$ . In each iteration, given  $n_q$  correspondences between  $N$  faces, we connect the corresponding points through Delaunay triangulation of the mean locations of the  $n_q$  points. Thus, we get the same triangulation for all faces. We pick pairs of parent and child nodes from the Minimum Spanning Tree  $\Pi$  and for each face in a pair, extract a geodesic patch  $\mathbf{S} = [x_i, y_i, z_i]^T \subset \mathbf{F}_j, i = 1, \dots, m$ , along each triangle edge (see Figure 4). Since the extraction of geodesic patch can be highly sensitive to the surface sampling or mesh resolution [41], the scale at which to extract a local geodesic patch becomes challenging. To mitigate this problem, for every edge, we first rotate the mesh along the  $Z$ -axis so that the  $y$ -coordinates of the endpoints of the edge lie on a straight horizontal line. Given two vertices  $\mathbf{v}_a = [x_a, y_a, z_a]^T$  and  $\mathbf{v}_b = [x_b, y_b, z_b]^T$ , the rotation angle is given by  $\theta_{rz} = (y_b - y_a)/(x_b - x_a)$ . The size of the extracted geodesic patch is a function of its length and width. After rigid rotation along the  $Z$ -axis, the length of the extracted geodesic patch is defined by the  $x$ -coordinates of the endpoints. To adjust the width, we define it as a multiple of the average mesh resolution ( $5\rho$ ) at the endpoints. Here,  $\rho$  is the average length of the edges within the immediate neighbourhood of the two end points. This makes the extraction of the geodesic patch scale invariant. We are mainly interested in extracting a surface patch wide enough to contain significant local curvature information for the detection of keypoints in the subsequent stage.

Finally, we register the extracted geodesic patches of the second face in the pair with the first one employing a non-rigid approach [42, 43].

#### 2.5. Keypoint Detection on Geodesic Patches

The aim of keypoint detection is to find discriminative points that facilitate accurate matches. Sun and Abidi [19, 20] used keypoints to select the candidate points for which face Finger Prints were calculated. The use of keypoints for establishing correspondences between different instances of the same objects is a well-established technique in 3D face/object recognition [44, 41]. However, the focus of



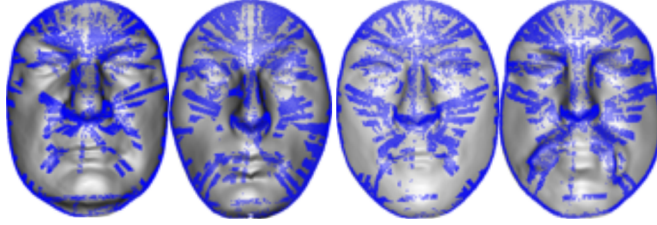


Figure 5: Illustration of keypoints (not corresponding points) detected along geodesic patches in the tenth iteration of our algorithm. Notice the repeatability of keypoints across the identities.

those applications is on discriminating identities and the features are specifically designed to capture information pertaining to the uniqueness of an identity. We propose a feature descriptor that is capable of matching keypoints across different individuals. Another characteristic of the keypoint detection in [44] is that the keypoints do not cover the whole face, but are concentrated around regions of high curvature/discrimination, e.g. mouth, nose, and eyes. However, this property is not desirable when dense correspondences are to be established over the complete face. We solve this problem by finding additional keypoints along geodesic patches i.e. by evolving level set geodesic curves and sampling equidistant points. Thus we are able to establish dense correspondences that cover the whole face by matching features at these points.

The input to our algorithm is the geodesic surface patch  $\mathbf{S}$  extracted between two vertices of a triangle. A smaller patch is cropped using a sphere of radius  $r_p$  at each sample point  $p$  of  $\mathbf{S}_j$ . Large values of  $r_p$  tend to capture the identity specific descriptiveness rather than the features of the local point[41]. Instead of fixing  $r_p$  as in [44], we calculate  $r_p = 5\rho$  (where  $\rho$  is the mesh resolution) to extract the local surface surrounding each sample point. Recall that  $5\rho$  is also the width of the geodesic patch. The values of  $\rho$  for real 3D faces captured with the Minolta<sup>TM</sup> or the 3dMDface<sup>TM</sup> scanners typically range from 1-3mm. Hence a value of  $5\rho$  keeps the extracted features local to the sample point  $p$ . Note that the value of  $\rho$  changes with every geodesic patch unlike existing techniques [45] where a single mesh resolution is used for object recognition.

Let  $\mathbf{G}_j = [x_i, y_i, z_i]^T$  (where  $i = 1, \dots, n_g$  and  $n_g$  are the total number of points in  $\mathbf{G}$ ) be the cropped pointcloud pertaining to the local surface centred at  $p$ . The mean of the pointcloud is  $\mu = \frac{1}{n_g} \sum_{i=1}^{n_g} \mathbf{G}_i$  and its covariance is  $\mathbf{C} = \frac{1}{n_g} \mathbf{G}_m^T \mathbf{G}_m$ , where  $\mathbf{G}_m$  is the mean-centred pointcloud. We perform Singular Value Decomposition (SVD) [46] of the covariance matrix  $\mathbf{U}\mathbf{D}\mathbf{V}^T = \mathbf{C}$  where  $\mathbf{U}$  and  $\mathbf{V}$  are two orthogonal matrices and  $\mathbf{D}$  is diagonal matrix of eigenvalues sorted in decreasing order. We use the ratio of the first two eigenvalues  $\frac{s_1}{s_2}$  for keypoint detection. Note that by default  $s_1 \geq s_2$  while  $s_1 = s_2$  signifies that the local surface  $\mathbf{G}_j$  is symmetric and not a suitable keypoint. We select  $p$  as a keypoint if the ratio  $\frac{s_1}{s_2} > t_k$ . We empirically found  $t_k = 1.2$  to be a good choice. Figure 5 shows keypoints detected by our algorithm in the tenth iteration on four different identities of the FRGCv2 database.

We use the keypoints detected on surface patch  $\mathbf{S}_j$  for feature extraction and matching only if an adequate number of keypoints are detected (minimum three for triangulation). Otherwise,  $\mathbf{S}_j$  is not considered to be sufficiently descriptive and further correspondences on this patch are established using an alternate method described in Section 2.7.



## 2.6. Feature Extraction and Matching

We denote  $\Psi_j = [x_i, y_i, z_i]^T, i = 1, \dots, n_\Psi$  as the set of keypoints detected on the surface  $\mathbf{S}_j$ , where  $n_\Psi$  is the number of keypoints. For each keypoint on the surface  $\mathbf{S}_j$  of both 3D faces in the ordered pair, we extract feature vectors  $\mathbf{x}_1^k$  and  $\mathbf{x}_2^l$  where  $k = 1, \dots, n_{\Psi_1}$  and  $l = 1, \dots, n_{\Psi_2}$ . The subscripts 1 and 2 denote the first and second 3D face in the ordered pair. The local surface  $r_x = 5\rho$  around each keypoint  $\Psi_j$  is used to extract a set of 3D signature and histogram based descriptors. These descriptors have been widely used in the literature [28, 45, 47] for automatic object recognition and for landmark detection. We use a combination of many descriptors since the surface patch is quite small and a single descriptor may not capture sufficient information. The list of descriptors is given below:

- The spatial location  $[x_i, y_i, z_i]^T$ .
- The surface normal  $[n_x, n_y, n_z]^T$ .
- The seven invariant moments [36] of the  $3 \times 3$  histograms of the  $XY, YZ$  and  $XZ$  planes.
- The central moment  $\mu_{mn}$  of order  $m + n$  of the histogram matrix  $\mathbf{H}$ :

$$\mu_{mn} = \sum_{i=1}^{\varphi} \sum_{j=1}^{\varphi} (i - \bar{i})^m (j - \bar{j})^n \mathbf{H}(i, j), \quad (3)$$

where  $\varphi$  is the total number of points in  $\mathbf{H}$ ,  $\bar{i} = \frac{1}{\varphi} \sum_{i=1}^{\varphi} \sum_{j=1}^{\varphi} i \mathbf{H}(i, j)$  and  $\bar{j} = \frac{1}{\varphi} \sum_{i=1}^{\varphi} \sum_{j=1}^{\varphi} j \mathbf{H}(i, j)$ .

- The mean of the two principle curvatures  $\bar{k}_1$  and  $\bar{k}_2$  calculated at each point on the extracted local surface
- The Gaussian Curvature  $K = k_1 k_2$
- The Mean Curvature  $H = \frac{k_1 + k_2}{2}$
- The Shape Index . We use two variants of the shape index which vary from 0 to 1 and  $-1$  to 1 respectively,

$$s_a = \frac{1}{2} - \frac{1}{\pi} \arctan \frac{k_1 + k_2}{k_1 - k_2}, \quad 0 \leq s_a \leq 1 \text{ and}$$

$$s_b = \frac{2}{\pi} \arctan \frac{k_1 + k_2}{k_1 - k_2}, \quad -1 \leq s_b \leq 1.$$

- The Curvedness  $c = \sqrt{\frac{k_1^2 + k_2^2}{2}}$
- The Log-Curvedness  $c_l = \frac{2}{\pi} \log \sqrt{\frac{k_1^2 + k_2^2}{2}}$ ,
- The Willmore Energy  $e_w = H^2 - K$ ,
- The Shape Curvedness  $c_s = s_b \cdot c_l$
- The Log Difference Map  $m_l = \ln(K - H + 1)$ .

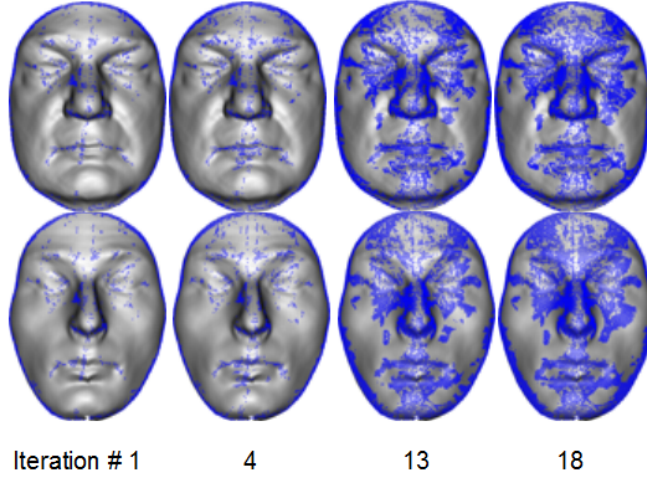


Figure 6: Correspondence established in 18 iterations of our algorithm on the first 2 identities of FRGCv2. Notice how well the points correspond across the identities.

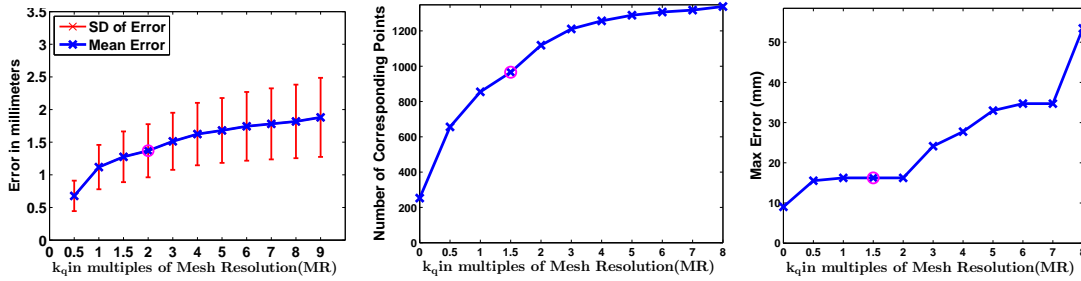


Figure 7: The effect of correspondence quality threshold  $k_q$  in the synthetic dataset in the first iteration. (Left) Graph of  $k_q$  vs the mean and SD of correspondence localization error. (Middle)  $k_q$  vs the number of correspondences established. (Right)  $k_q$  vs the maximum localization error. For all our experiments we have set  $k_q = 2\rho$  shown in the graphs in a magenta circle.

Using these descriptors, the dimensionality of the final feature vector  $\mathbf{x}_k$  is 38. These features are extracted over a small enough local surface centred at the keypoint such that they are repeatable across identities. In contrast, the feature vector extracted by Mian et al. [44, 41] takes the range values of a larger surface (typically 20mm radius) surrounding each keypoint. Hence, their features are repeatable only over the same identity. One of the prerequisites of the techniques that use depth values as features [44, 41, 45, 47] is to define a local reference frame for pose invariant matching. In our case, the features are either already pose invariant and hence do not require a local reference frame.

Next, we perform constrained-NN search between the feature vectors  $\mathbf{x}_1^k$  and  $\mathbf{x}_2^l$  such that the corresponding points lie within a certain proximity to each other. To avoid large errors in establishing correspondence between two points, we set a threshold of  $k_q$  to define the neighbourhood. Hence, keypoints  $k$  and  $l$  from both 3D faces in the ordered pair are accepted as corresponding points if their cost  $\Sigma_{kl} \leq k_q$ , where the cost function is defined as,

$$\Sigma_{kl} = \|\mathbf{x}_1^k - \mathbf{x}_2^l\|_2^2 \quad (4)$$

The quality of correspondence varies directly with  $k_q$ . Higher values of  $k_q$  will result in poor corresponding points with large errors, whereas lower values of  $k_q$  may reject valid correspondences and

hence adversely effect the correspondence density. We set the value of  $k_q = 2\rho$  which is a standard threshold used in many 3D object recognition algorithms [48]. Figure 7 shows the effect of  $k_q$  on the correspondence found in our experiments on the synthetic dataset. As we increase the value of  $k_q$ , the mean localization error and its standard deviation increases.

We also note the quality of a corresponding point which is the value of the cost function  $\Sigma_{kl}$  at which correspondence of that point was established. Figure 6 shows the outcome of this step on two identities.

Once corresponding points have been detected on all surfaces  $\mathbf{S}_j$  of the complete data set in the pairwise scheme, we select  $n_q$  corresponding points with the smallest value of their respective cost function  $\Sigma_{kl}$  (4) as seed corresponding points for the next iteration. Selecting the best matches as seed points reduces computational cost for the subsequent iteration. This step also reduces overlaps with already established corresponding points and ensures propagation of accurate correspondences. We use a value of  $n_q = 80$  in our experiments. Next, we obtain a triangulation of these points on the mean face of the dataset and extract geodesic surface patches as described in Section 2.4. The output of this step is a set of corresponding faces  $\tilde{\mathbf{F}}_j = [x_p, y_p, z_p]^T$ , where  $j = 1, \dots, N$  and  $p = 1, \dots, \hat{P}$ . Note that while only  $n_q$  best quality corresponding points are selected for triangulation in the next iteration, the rest of the corresponding points are retained as valid correspondences. Algorithm 1 details the process of establishing dense correspondence using keypoints.

### 2.7. Level Set Geodesic Curves based Correspondence on Less-descriptive Geodesic Patches

Keypoints signify areas that are non-symmetric on geodesic patches along the edges of triangulation connectivity in each iteration. After a few iterations, most keypoints on the face are detected and either accepted as corresponding points after feature matching or discarded. However, there are still areas on the 3D faces where correspondence has not been established because of the lack of keypoints. These surfaces are either symmetric or devoid of high curvatures. A simple approach to establish dense correspondence in these areas would be to sample them uniformly across the complete dataset. Such an approach has been used in 2D by Munsell et al. [49] who pre-organized the shape instances based on a similarity measure and then established correspondence between pairs of shapes by mapping the points from the source instance to the target instance after minimizing a bending energy. However, in 3D faces this approach requires the portions of 3D faces to be planar or spherical (which is hardly the case) and hence would result in large correspondence errors.

We propose a solution for establishing correspondences in areas which are devoid of high curvatures. After triangulation of the final set of best quality corresponding points, we select large triangles with area greater than  $t_a$ . A simple value for  $t_a$  is the mean area of all triangles in the connectivity. This threshold is a measure to reduce computational cost and as such has no bearing on the technique. From the centroid of each triangle, we evolve a geodesic curve with a uniform speed function. For this purpose we follow the Fast Marching Method [50] and use the implementation given by Peyre [51]. We then sample the points on the curve at regular intervals to obtain equidistant points (see Figure 8). Since, the evolution of a geodesic curve is sensitive to curvature, a uniform speed function on smooth and planar areas ensures sampling of surface points that are equidistant and correlated within the same triangle on all 3D faces of the dataset. In order to densely sample the points in a triangle, we allow the curve to spill

---

**Algorithm 1** Keypoint Based Dense Correspondence

---

**Require:** Faces  $\mathbf{F}_j = [x_p, y_p, z_p]^T$  where  $p = 1, \dots, P_j$  and  $j = 1, \dots, N$ , Minimum Spanning Tree

$$\Pi = (V_t, E_t).$$

**Initialization:**

- 1: Find seed corresponding points  $\mathbf{L} = \{\iota_1, \dots, \iota_N\}$  where  $\iota_n = [x_k, y_k, z_k]^T$ , and  $k = 1, \dots, \frac{2\pi}{\delta}$
  - 2:  $\tilde{\mathbf{F}}^j \leftarrow \iota_j, j = 1, \dots, N$ . Set each corresponded 3D face to initial corresponding points
  - 3:  $n_q = \frac{2\pi}{\delta}$
  - 4: Iteration:  $i = 0$
  - 5: **while**  $n_\Psi > t_1$  **do**
  - 6:    $n_\Psi = 0$
  - 7:   Update iteration:  $i = i + 1$
  - 8:   **for**  $\forall(\mathbf{F}_a, \mathbf{F}_b | a \neq b)$  in  $\Pi$  **do**
  - 9:     Triangulate over  $n_q$  corresponding points
  - 10:    **for** all triangle edges  $n_e$  **do**
  - 11:     Extract geodesic patch  $\mathbf{S}_1 \subset \mathbf{F}_a$  and  $\mathbf{S}_2 \subset \mathbf{F}_b$
  - 12:     Detect keypoints  $\Psi_1 \subset \mathbf{S}_1$  and  $\Psi_2 \subset \mathbf{S}_2$
  - 13:      $n_\Psi = n_\Psi + \min(n_{\Psi_1}, n_{\Psi_2})$
  - 14:     Extract features  $\mathbf{x}_1^k$  and  $\mathbf{x}_2^l$  around each keypoint in  $\Psi_1$  and  $\Psi_2$ ,  $k = 1, \dots, n_{\Psi_1}$ ,  $l = 1, \dots, n_{\Psi_2}$
  - 15:      $\Sigma_{kl} = \|\mathbf{x}_1^k - \mathbf{x}_2^l\|_2^2$
  - 16:      $\tilde{\mathbf{F}}_a \leftarrow \{\tilde{\mathbf{F}}_a \cup \Psi_1^k\}$  and  $\tilde{\mathbf{F}}_b \leftarrow \{\tilde{\mathbf{F}}_b \cup \Psi_2^l\}$  if  $\Sigma_{kl} \leq k_q$
  - 17:    **end for**
  - 18:   **end for**
  - 19:   Select  $n_q$  corresponding points for triangulation
  - 20: **end while**
  - 21: **return**  $\tilde{\mathbf{F}}_j = [x_p, y_p, z_p]^T$  where  $p = 1, \dots, \hat{P}$ .
- 

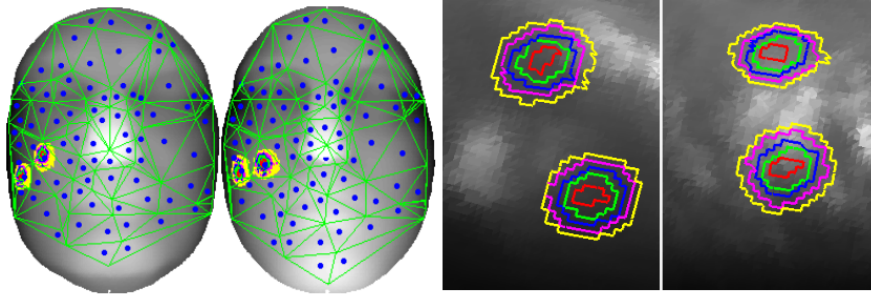


Figure 8: Correspondence establishment on smooth surfaces. Two faces from an ordered pair with triangulation over  $n_q$  best quality corresponding points. Blue dots indicate the centroids of large triangles. Level set based evolution of geodesic curves for the two sample triangles, magnified on the right.

over the boundaries but only select points that are inside. Although these points are not keypoints, they are repeatable on all 3D faces across identities because they are extracted from triangles whose vertices are corresponding to each other across the dataset. Furthermore, these points are extracted at equal intervals over a small region which is smooth. From this set of points, correspondence is established by extracting and matching feature vectors (see Section 2.6). This is not an iterative process and points are sampled only once from each triangle meeting the threshold criterion. Feature matching ascertains that only points with a minimum cost  $\Sigma_{kl}$  (4) are selected to ensure accurate correspondences. Figure 8 visually illustrates the process. Finally, the dense corresponding faces  $\tilde{\mathbf{F}}_j = [x_p, y_p, z_p]^T, j = 1, \dots, N$  and  $p = 1, \dots, P$  ( $P > \hat{P}$ ) are updated with the newly established corresponding points.

### 3. K3DM Fitting and Augmentation

The output of the dense correspondence algorithm is the set of  $N$  densely corresponding 3D faces  $\tilde{\mathbf{F}}_j$  which form our Keypoints based 3D Deformable Model (K3DM)  $\Upsilon = [\tilde{\mathbf{f}}_1, \tilde{\mathbf{f}}_2, \dots, \tilde{\mathbf{f}}_N, ]$ , where  $\tilde{\mathbf{f}} = [x_1, \dots, x_p, y_1, \dots, y_p, z_1, \dots, z_p]^T$  and  $p = 1, \dots, P$ . The row mean  $\boldsymbol{\mu}_\Upsilon$  of the K3DM is given by,

$$\boldsymbol{\mu}_\Upsilon = \frac{1}{N} \sum_{i=1}^N \tilde{\mathbf{f}}_i \quad (5)$$

The row-normalized model  $\Upsilon_m = \Upsilon - \boldsymbol{\mu}_\Upsilon$  can be modelled by a multivariate Gaussian distribution and its eigenvalue decomposition is given by,

$$\mathbf{U}\mathbf{S}\mathbf{V}^T = \Upsilon_m \quad (6)$$

where  $\mathbf{U}\mathbf{S}$  are the principal components (PCs), and the columns of  $\mathbf{V}$  are their corresponding loadings.  $\mathbf{S}$  is a diagonal matrix of eigenvalues and we retain 98% of the energy corresponding to the first  $n$  columns of  $\mathbf{U}$ .

We propose to deform the statistical model given in (6) into a query face  $\mathbf{Q}$  in a two step iterative process, i.e. registration and morphing. Algorithm 2 gives the details of fitting the deformable model to query face. The query face after vectorization can be parametrized by the statistical model such that  $\tilde{\mathbf{q}} = \mathbf{U}\boldsymbol{\alpha}^i + \boldsymbol{\mu}_\Upsilon$ , where the vector  $\boldsymbol{\alpha}^i$  contains the parameters which are used to vary the shape of the model in the  $i^{th}$  iteration and  $\tilde{\mathbf{q}}$  is the vectorized form of the query face  $\tilde{\mathbf{Q}}$ . In the initialization step  $\boldsymbol{\alpha}^i$  is set to zero and the deformable model  $\mathbf{M}^i$  is characterized by the mean face of the K3DM. Each iteration begins with a registration step where the input face  $\mathbf{Q}$  is registered to the model  $\mathbf{M}^i$ . This step essentially entails finding an approximate nearest neighbour correspondence between the model and the query face and a rigid transformation. Correspondence is established by searching for the Nearest Neighbour (NN) of each point of  $\mathbf{M}^i$  in  $\mathbf{Q}$  using the k-d tree data structure [52]. Let  $\mathbf{d}$  represent the NN Euclidean distance between the corresponded query face and the model such that  $d_j = \|\tilde{\mathbf{Q}}^i - \mathbf{M}^i\|_2^2$ . We define outliers as points on  $\tilde{\mathbf{Q}}$  whose NN distance with  $\mathbf{M}^i$  is greater than a threshold  $t_c$  where  $t_c = \bar{\mathbf{d}} + 3\sigma_d$  and exclude them from registration. This step ensures that the outliers do not affect the registration process. Next, the query face is translated to the mean of the model and is rotated to align with  $\mathbf{M}^i$ . The rotation

matrix is found by taking the PCA of the covariance matrix  $(\tilde{\mathbf{Q}} - \boldsymbol{\mu}_Q)(\mathbf{M}^i - \boldsymbol{\mu}_M)^T$  where  $\tilde{\mathbf{Q}}$  is the query face containing only the corresponding points. The eigenvectors of the PCA give us the rotation matrix. We denote the corresponded and registered query face by  $\mathbf{Q}_r$ . Note that we use  $\mathbf{Q}$  and  $\mathbf{M}$  for the point clouds of the query face and model and use  $\mathbf{q}$  and  $\mathbf{m}$  for their vectorized versions respectively.

In the next step, the model  $\mathbf{M}^i$  is deformed to fit the registered query face  $\mathbf{Q}_r$  such that,

$$\hat{\boldsymbol{\alpha}}^i \Leftarrow \min_{\boldsymbol{\alpha}^i} \|\mathbf{U}^* \boldsymbol{\alpha}^i + \boldsymbol{\mu}_\Upsilon - \mathbf{q}_r\|_2^2 + \lambda \|\boldsymbol{\alpha}^i - \boldsymbol{\alpha}^{i-1}\|_2 \quad (7)$$

and  $\mathbf{m}^i = \mathbf{U} \hat{\boldsymbol{\alpha}}^i + \boldsymbol{\mu}_\Upsilon$ . The \* denotes that only those points (rows of  $\mathbf{U}$  and  $\boldsymbol{\mu}_\Upsilon$ ) are considered which satisfy the threshold  $t_c$ . The second term in (7) puts a constraint on deforming the model. The applied condition is intuitive because we want to partially deform the model in each iteration such that the model approximates the query face in small steps. The iterative procedure is terminated when the residual error  $\|\mathbf{m}^i - \mathbf{q}_r\|_2^2 \leq \epsilon_f$ . In all of our experiments  $\lambda$  was set to 0.8 and  $\epsilon_f = 10^{-4}$ .

---

**Algorithm 2** K3DM Fitting

---

**Require:**  $\Upsilon_m = [\tilde{\mathbf{f}}_1, \tilde{\mathbf{f}}_2, \dots, \tilde{\mathbf{f}}_N] - \boldsymbol{\mu}_\Upsilon$  and Query Face  $\mathbf{Q} = [x_p, y_p, z_p]^T$  where  $p = 1, \dots, P_q$ .

**Initialization:**

- 1: Iteration:  $i = 0$
  - 2:  $\mathbf{USV}^T = \Upsilon_m$
  - 3:  $\boldsymbol{\alpha}^i = 0$
  - 4:  $\mathbf{m}^i = \mathbf{U} \boldsymbol{\alpha}^i + \boldsymbol{\mu}_\Upsilon$
  - 5:  $\epsilon^0 = 1$
  - 6: **while**  $\epsilon^i > \epsilon_f$  **do**
  - 7:   Update iteration:  $i = i + 1$
  - 8:    $\tilde{\mathbf{Q}} = \mathbf{Q} \Leftarrow \mathbf{M}^i$  (NN using k-d tree)
  - 9:    $\tilde{\mathbf{Q}}' = \{\tilde{\mathbf{Q}} \mid \|\tilde{\mathbf{Q}}^i - \mathbf{M}^i\|_2^2 < \bar{\mathbf{d}} + 3\sigma_d\}$
  - 10:    $\mathbf{Q}_r = \tilde{\mathbf{Q}}' \mathbf{R} + \mathbf{t}$  (Registration step)
  - 11:    $\mathbf{U}^* \Leftarrow \{ \mathbf{U} \mid \text{rows of } \mathbf{U} \text{ correspond to } \tilde{\mathbf{Q}}' \}$
  - 12:    $\hat{\boldsymbol{\alpha}}^i \Leftarrow \min_{\boldsymbol{\alpha}^i} \|\mathbf{U}^* \boldsymbol{\alpha}^i + \boldsymbol{\mu}_\Upsilon - \mathbf{q}_r\|_2^2 + \lambda \|\boldsymbol{\alpha}^i - \boldsymbol{\alpha}^{i-1}\|_2$
  - 13:    $\mathbf{m}^i = \mathbf{U} \hat{\boldsymbol{\alpha}}^i + \boldsymbol{\mu}_\Upsilon$
  - 14:    $\epsilon^i = \|\mathbf{m}^i - \mathbf{q}_r\|_2^2$
  - 15: **end while**
  - 16: **return**  $\mathbf{Q}_r, \hat{\boldsymbol{\alpha}}, \mathbf{m}$
- 

From a practical perspective, there is usually a need to augment an existing dense correspondence model with new 3D faces. In the following, we present a K3DM augmentation algorithm to achieve this objective. Given the K3DM and a batch of  $M$  new 3D faces, we compute the bending energy required to deform the mean face of the K3DM to each of the new faces. This information is employed to organize the  $M$  faces in a Minimum Spanning Tree as outlined in Section 2.2. Traversing from the root node (mean face), the K3DM is morphed into each child node using the model fitting procedure given in Algorithm 2. The resulting corresponded 3D face of the input identity is added to the K3DM. Algorithm 3 gives the details of our model augmentation technique.

---

**Algorithm 3** K3DM Augmentation

---

**Require:**  $\Upsilon = [\tilde{\mathbf{f}}_1, \tilde{\mathbf{f}}_2, \dots, \tilde{\mathbf{f}}_N]$  and a batch of input 3D faces  $F_M = \{\mathbf{f}_1, \mathbf{f}_2, \dots, \mathbf{f}_M\}$  where  $\mathbf{f}_i = [x_1, \dots, x_p, y_1, \dots, y_p, z_1, \dots, z_p]^T$ ,  $p = 1, \dots, P_M$  and  $M \geq 1$ .

**Initialization:**

- 1: Pre-organize the  $M$  faces in a Minimum Spanning Tree  $\Pi = (V_t, E_t)$
  - 2: **for** each 3D face  $\mathbf{f}_i$  in  $\Pi$  **do**
  - 3:    $\tilde{\mathbf{f}}_i = \text{fit\_K3DM}(\Upsilon, \mathbf{f}_i)$
  - 4:    $\Upsilon = [\tilde{\mathbf{f}}_1, \tilde{\mathbf{f}}_2, \dots, \tilde{\mathbf{f}}_N, \tilde{\mathbf{f}}_i]$
  - 5:   Increment number of faces in the model
  - 6:    $\mu_\Upsilon = \frac{1}{N} \sum_{n=1}^N \Upsilon_n$
  - 7: **end for**
  - 8: **return**  $\Upsilon = [\tilde{\mathbf{f}}_1, \tilde{\mathbf{f}}_2, \dots, \tilde{\mathbf{f}}_{N+M}]$
- 



Figure 9: Qualitative results of our dense correspondence algorithm on the first 3 identities of FRGCv2. The first face in each row is the source and the last face is the target. Notice the smooth morphing between source and target faces even in the presence of small pose variations (row 2).

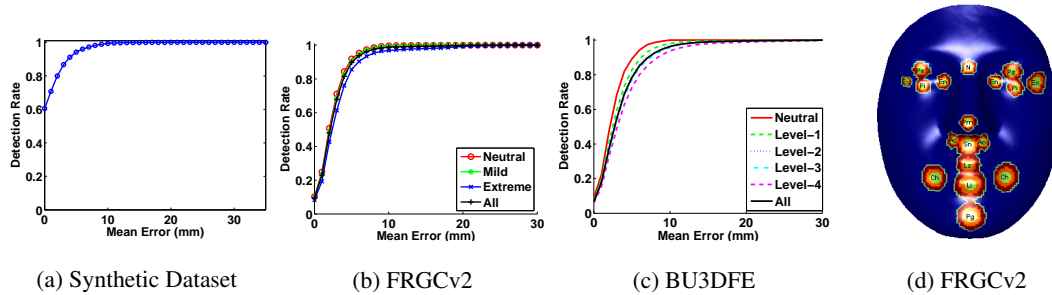


Figure 10: Results of dense correspondence: (a-c) Cumulative localization error distribution plots on the Synthetic (2,246 vertices), FRGCv2 (18 landmarks), and BU3DFE (12 landmarks) datasets. (d) Distribution of correspondence error of each landmark on FRGCv2. The three circles show areas corresponding to mean error ( $\mu_e$ ),  $\mu_e + SD$  and  $\mu_e + 2SD$  respectively.



## 4. Experimental Setup

We have carried out extensive experiments on synthetic and real data. Below are the details of the datasets used, evaluation criteria and the experiments performed.

### 4.1. Datasets Used

Our synthetic dataset consists of 100 3D faces generated from the Facegen software<sup>1</sup>. Facegen has been used by scientists in the field of neuroscience and social cognition to generate synthetic faces for replicating human stimuli [53, 54]. The 100 faces are in perfect correspondence with each other and hence provide the ground truth. Each face has 3,727 vertices and 7,179 triangles. For experiments on real 3D faces, we used the FRGCv2 [27] and BU3DFE [24] datasets. FRGCv2 contains 4,007 scans of 466 individuals. The dataset contains scans with expressions ranging from mild to extreme as well as multiple ethnicities. Similarly, BU3DFE database consists of 2,500 scans of 100 individuals. Each individual has been imaged in one neutral and six non-neutral expressions at four intensity levels each. Both datasets have a pose variations of  $\pm 10^\circ$ .

### 4.2. Evaluation Criteria

One of the major challenges in evaluating the results of shape-correspondence algorithms is the absence of an objective evaluation technique. For real life data, the main reason for this challenge is the unavailability of the ground-truth shape correspondence [55]. A solution to this problem is the use of synthetic dataset where correspondences are known a priori. We used the synthetic 3D face dataset as ground truth for our evaluations and to the best of our knowledge, this is the first time synthetic 3D face images have been used to evaluate results of a dense correspondence algorithm in terms of mean localization error of the corresponded points. For the real life data sets, reporting the localization error over densely corresponding points is not practical because it is humanly not feasible to annotate thousands of unique ground truth landmarks on each face. Hence in this case, we report the mean localization error over a sparse set of anthropometric landmarks and compare the results with the state-of-the-art automatic landmark detecting algorithms.

Objective measures for evaluating the dense correspondence accuracy together with the deformable model fitting algorithm is its application to face recognition and gender classification. Results on these applications are expected to be better when the underlying models have accurate dense correspondences. Hence, we used our dense correspondence models and fitting algorithm in these applications and evaluated the results.

Furthermore, the correspondence quality can be subjectively evaluated by inspecting the morph between faces. A smooth transition between corresponding faces is indicative of accurate correspondences [34, 56]. Figure 9 shows the qualitative results of our dense correspondence algorithm. Smooth transition of one face to the other indicates high quality dense correspondences between the 3D faces.

---

<sup>1</sup>Singular Inversions, "Facegen Modeller", [www.facegen.com](http://www.facegen.com)

Table 1: Landmark localization error ( $\epsilon_L$ ) in mm on FRGCv2 dataset. We have used the anatomic names and conventions for these landmarks from [1].

Expression	Neutral Expression(n=1,947)			Mild Expression(n=936)			Extreme Expression(n=1,124)			All (n=4,007)		
$\epsilon_L$	Mean	SD	$\leq 10mm(\%)$	Mean	SD	$\leq 10mm(\%)$	Mean	SD	$\leq 10mm(\%)$	Mean	SD	$\leq 10mm(\%)$
<b>Ex(R)</b>	2.29	0.84	100.00	2.32	0.84	100.00	2.51	0.92	100.00	2.36	0.87	100.00
<b>En(R)</b>	2.30	1.62	99.74	2.27	1.75	99.68	2.59	1.86	99.73	2.37	1.72	99.73
<b>Ps(R)</b>	2.59	1.73	99.79	2.81	1.79	99.79	3.01	2.08	99.38	2.76	1.86	99.68
<b>Pi(R)</b>	2.31	1.49	99.95	2.46	1.57	99.79	2.65	1.69	99.73	2.44	1.57	99.85
<b>N</b>	2.61	1.47	100.00	2.52	1.50	100.00	2.80	1.61	100.00	2.64	1.52	100.00
<b>Ex(L)</b>	2.31	1.49	99.85	2.37	1.61	99.57	2.67	1.82	99.47	2.43	1.62	99.68
<b>En(L)</b>	3.56	2.15	99.08	3.88	2.30	98.29	4.32	2.62	97.06	3.85	2.35	98.33
<b>Ps(L)</b>	2.99	1.99	99.59	3.24	2.11	99.57	3.37	2.38	98.75	3.15	2.14	99.35
<b>Pi(L)</b>	2.61	1.67	99.79	2.59	1.71	99.79	2.92	1.90	99.73	2.69	1.75	99.78
<b>Prn</b>	2.44	1.87	99.38	2.51	1.83	99.47	2.67	1.84	99.82	2.52	1.85	99.53
<b>Ac(R)</b>	2.20	1.70	99.74	2.29	1.59	99.79	2.58	2.21	98.75	2.32	1.84	99.48
<b>Sn</b>	3.00	2.04	100.00	2.90	2.16	98.93	4.35	4.44	92.53	3.35	3.00	97.65
<b>Ac(L)</b>	2.44	1.50	99.64	2.57	1.67	99.36	2.86	2.09	98.58	2.59	1.73	99.28
<b>Ch(R)</b>	3.53	2.26	99.02	3.77	2.33	98.61	5.10	4.06	92.88	4.03	2.97	97.20
<b>Ch(L)</b>	3.51	2.37	98.36	3.55	2.23	99.25	5.10	4.85	91.90	3.97	3.31	96.76
<b>Ls</b>	2.21	1.80	99.90	2.59	2.02	99.68	4.20	4.84	93.15	2.86	3.13	97.95
<b>Li</b>	3.40	3.09	96.82	3.98	3.58	93.48	5.39	4.94	85.85	4.09	3.89	92.96
<b>Pg</b>	3.74	2.45	100.00	3.71	2.39	100.00	4.88	4.63	92.26	4.05	3.25	97.83
<b>Mean Error</b>	2.78	0.60	99.48	2.91	0.61	99.17	3.55	0.91	96.64	3.03	0.78	98.61

## 5. Results and Analysis

### 5.1. Landmark Localization

**Synthetic Dataset:** First, we present the evaluation of our algorithm on synthetic data. We establish dense correspondence on 100 synthetic 3D faces using our proposed algorithm and report the mean and the standard deviation of the localization error with respect to the ground truth.

The original synthetic dataset contains 3,727 vertices for each 3D face. Our proposed method is successful in establishing dense correspondence over 2,246 vertices (60% of the original) with a mean localization error of 1.28mm and SD  $\pm 2.2mm$ . Correspondence within 10mm is established on 99.33% vertices. Figure 10(a) shows a plot of the cumulative distribution of correspondences within a given error distance.

**FRGCv2 Dataset:** We construct a dense correspondence K3DM from the first available neutral scan of the first 200 identities (100 males and females each) of FRGCv2. All scans of the remaining 266 identities (1,956 in total) are used as the test set. In the next step, we construct a K3DM from the neutral scans of the next 200 identities (100 male and female each) and use all the scans (2,051) corresponding to the first training set as probes. In this way we report Landmark Detection results on all 4,007 scans of FRGCv2, each time ensuring that the identity in the gallery is not present in the probe.

Our proposed algorithm establishes dense correspondences between 9,309 vertices on the FRGCv2 dataset. We report the mean and standard deviation of the Landmark Localization Error ( $\epsilon_L$ ) on 18 fiducial points considered to be biologically significant [1]. These anthropometric landmarks are annotated

Table 2: Comparison of the mean (mm) and standard deviation (mm) of  $\epsilon_L$  with state of the art algorithms on FRGCv2 dataset. A ‘-’ denotes that the authors have not detected this particular landmark.

Mean of Landmark Localization Error (mm)															
Author	# Images	Ex(L)	En(L)	N	Ex(R)	En(R)	Prn	Ac(L)	Ac(R)	Ch(L)	Ch(R)	Ls	Li	Pg	Sn
Lu et al. [25]	676	9.50	8.20	-	10.30	8.30	8.30	-	-	6.00	6.20	-	-	-	-
Segundo et al. [26]	4007	-	3.69	-	-	3.35	2.73	4.83	5.84	-	-	-	-	-	-
Perakis et al. [29]	975	5.38	3.95	-	-	4.37	3.99	-	-	4.25	4.35	-	-	-	-
Creusot et al. [28]	4007*	5.87	4.31	4.20	6.00	4.29	3.35	4.73	4.86	5.47	5.64	4.23	5.46	7.28	3.67
<b>This Paper</b>	4007	3.85	2.43	2.64	2.37	2.36	2.52	3.97	4.03	2.59	2.32	2.86	4.09	4.05	3.35
Standard Deviation of Landmark Localization Error (mm)															
Author	# Images	Ex(L)	En(L)	N	Ex(R)	En(R)	Prn	Ac(L)	Ac(R)	Ch(L)	Ch(R)	Ls	Li	Pg	Sn
Lu et al. [25]	676	17.10	17.20	-	18.10	17.20	19.40	-	-	-	-	-	-	-	-
Segundo et al. [26]	4007	-	2.26	-	-	2.33	1.39	2.03	1.73	16.90	17.90	-	-	-	-
Perakis et al. [29]	975	3.14	2.19	-	3.37	2.51	2.24	-	-	2.30	2.40	-	-	-	-
Creusot et al. [28]	4007*	3.11	2.44	2.07	3.03	2.03	2.00	3.68	3.54	3.45	3.58	3.21	3.92	7.41	3.11
<b>This Paper</b>	4007	2.35	1.62	1.52	1.72	0.87	1.85	3.31	2.97	1.73	1.84	3.13	3.89	3.25	3.00

\* Algorithm was tested on 4,750 images. We have reported results on the 4,007 faces matching our dataset.

Table 3: Comparative results of our proposed algorithm with method SIS-NPSS [29] reported on *DB00F* [29]. Our dense correspondence algorithm is able to localize all landmarks with lower error.

Expression	Neutral (n=443)		Mild (n=355)		Extreme (n=177)		All (n=975)	
	SISI-NPSS	This Paper	SISI-NPSS	This Paper	SISI-NPSS	This Paper	SISI-NPSS	This Paper
$\epsilon_L$	Mean $\pm$ SD	Mean $\pm$ SD	Mean $\pm$ SD	Mean $\pm$ SD	Mean $\pm$ SD	Mean $\pm$ SD	Mean $\pm$ SD	Mean $\pm$ SD
<b>Ex(R)</b>	5.38 $\pm$ 3.14	2.27 $\pm$ 0.82	5.76 $\pm$ 3.42	2.38 $\pm$ 0.86	5.71 $\pm$ 3.57	2.54 $\pm$ 0.88	5.58 $\pm$ 3.33	2.36 $\pm$ 0.85
<b>EN(R)</b>	3.95 $\pm$ 2.19	2.33 $\pm$ 1.80	4.28 $\pm$ 2.35	2.46 $\pm$ 1.69	4.38 $\pm$ 2.68	2.64 $\pm$ 1.75	4.15 $\pm$ 2.35	2.44 $\pm$ 1.75
<b>En(L)</b>	4.37 $\pm$ 2.51	2.41 $\pm$ 1.50	4.48 $\pm$ 2.33	2.41 $\pm$ 1.66	4.40 $\pm$ 2.74	3.01 $\pm$ 2.08	4.41 $\pm$ 2.49	2.52 $\pm$ 1.69
<b>Ex(R)</b>	5.66 $\pm$ 3.37	4.00 $\pm$ 2.13	5.95 $\pm$ 3.38	4.13 $\pm$ 2.17	6.02 $\pm$ 3.59	4.97 $\pm$ 2.52	5.83 $\pm$ 3.42	4.22 $\pm$ 2.25
<b>Prn</b>	3.99 $\pm$ 2.24	2.94 $\pm$ 1.90	3.92 $\pm$ 2.06	2.95 $\pm$ 2.07	4.67 $\pm$ 3.25	3.13 $\pm$ 1.74	4.09 $\pm$ 2.41	2.98 $\pm$ 1.93
<b>Ch(R)</b>	4.25 $\pm$ 2.30	3.33 $\pm$ 2.14	5.36 $\pm$ 3.10	3.92 $\pm$ 2.54	9.26 $\pm$ 5.88	6.77 $\pm$ 4.78	5.56 $\pm$ 3.93	4.17 $\pm$ 3.18
<b>Ch(L)</b>	4.35 $\pm$ 2.40	3.24 $\pm$ 2.22	5.21 $\pm$ 3.14	3.34 $\pm$ 2.67	8.55 $\pm$ 5.87	4.75 $\pm$ 4.80	5.42 $\pm$ 3.84	3.55 $\pm$ 3.05
<b>Pg</b>	4.21 $\pm$ 2.36	3.70 $\pm$ 2.39	4.66 $\pm$ 2.70	3.91 $\pm$ 2.85	7.27 $\pm$ 6.45	4.18 $\pm$ 3.50	4.92 $\pm$ 3.74	3.86 $\pm$ 2.79
<b>Mean Error</b>	4.52 $\pm$ 1.51	3.03 $\pm$ 0.78	4.95 $\pm$ 1.46	3.19 $\pm$ 0.83	6.28 $\pm$ 2.60	3.99 $\pm$ 1.19	5.00 $\pm$ 1.85	3.26 $\pm$ 0.95

on the mean face and then projected back on each densely corresponded scan in the dataset. The manual annotations can be made on any dense corresponding scan without prejudice to the results. Manual annotations provided by Szeptycki et al. [57] and Creusot et al. [28] were used as ground truth for comparison. Since we manually classified the expressions in this dataset, we are able to report the results separately on each expression. Table 1 details the mean and standard deviation of  $\epsilon_L$  over 18 landmarks. Percentage of landmarks falling within a bound of  $10mm$  are also given. The same is shown graphically in Figure 10(b). The mean and standard deviation of  $\epsilon_L$  increases in the lower face region which is most affected by expressions. It is intuitive that the dispersion of error in the eyes and nose region as shown in Figure 10(d) is compact as compared to its wide distribution in the mouth region. The same is reflected by the ‘‘Extreme’’ expression results in Table 1. Over all, the mean localization error of the 18 landmarks on 4,007 scans is only  $3mm$ .

A comparison of the mean and standard deviation of  $\epsilon_L$  of our proposed algorithm with state-of-the-art algorithms in Table 2 makes it evident that our results outperform them by a significant margin. In

Table 4: Comparison of landmark localization results with the state-of-the-art on BU3DFE dataset. We have also reported the error rates for the landmarks which are most effected (mouth region) by expression [2].

Mean of Localization Error (mm)														
Author	# Images	Ex(L)	En(L)	N	Ex ( R )	En ( R )	Prn	Ac(L)	Ac ( R )	Ch(L)	Ch(R)	Ls	Li	Mean
Nair et al. [2]	2350	-	12.11	-	-	11.89	8.83	-	-	-	-	-	-	8.83
Segundo et al. [26]	2500	-	6.33	-	6.33	-	1.87	6.49	6.66	-	-	-	-	5.34
Salazar et al. [23]	350	9.63	6.75	-	8.49	6.14	5.87	6.47	7.17	-	-	-	-	6.83
<b>This Paper</b>	2500	3.96	2.84	4.33	3.65	2.66	2.59	2.81	2.95	5.63	5.22	3.79	6.96	4.03
Standard Deviation of Localization Error (mm)														
Author	# Images	Ex(L)	En(L)	N	Ex ( R )	En ( R )	Prn	Ac(L)	Ac ( R )	Ch(L)	Ch(R)	Ls	Li	Mean
Segundo et al. [26]	2500	-	4.82	-	-	5.04	1.12	3.36	3.40	-	-	-	-	3.55
Salazar et al. [23]	350	6.12	4.54	-	5.82	4.21	2.70	3.30	3.07	-	-	-	-	4.25
<b>This paper</b>	2500	2.39	1.58	2.65	2.39	1.69	1.77	1.89	1.80	3.66	3.41	2.37	6.63	2.69

Table 3, we make a detailed comparison with the SISI-NPSS method proposed by Perakis et al. [29]. Their test set contained 975 frontal scans of 149 identities and was further classified into “neutral”, “mild” and “extreme” expression subclasses. Since the information on these datasets is publicly available, we follow the exact protocols to have a fair comparison. Note that the authors used 300 scans with varying expressions to train their FLMs. In contrast, we have used only 200 neutral expression scans in our dense correspondence model. The mean localization error of our proposed algorithm for the eight reported points is  $3.26mm$  which is lower than  $5mm$  reported by Perakis et al. [29].

**BU3DFE Dataset:** We construct a dense correspondence model from the neutral scans of the first 200 identities of FRGC (first training set of Section 5.1) and tested on all 2,500 scans of the 100 identities of BU3DFE database. Landmark localization on BU3DFE dataset is more challenging because we use the K3DM of a different dataset for training. The results, however, are par excellence. To the best of our knowledge this is the first paper that reports results on BU3DFE database by training on scans from FRGCv2. We report mean and standard deviation of  $\epsilon_L$  on 12 anthropometric landmarks on all 2,500 scans of the dataset. Ground truth is provided with the database [24]. Table 4 shows the landmark localization results of our proposed algorithm and compares them with the state-of-the-art. Each identity in the BU3DFE dataset has been scanned in six different expressions with four intensity levels. Figure 10(c) shows the commutative detection rate of the 12 landmarks on all 2,500 scans.

## 5.2. Gender Classification

Facial gender classification is a non-trivial task because gender itself is a continuum [58]. Researchers have used sparse sets of corresponding points to extract various features for performing gender classification [59, 60, 61, 62]. We use our proposed algorithm to build a dense correspondence model and morph it into the query faces of FRGCv2 and BU3DFE dataset. We follow the same protocol of creating the K3DM as in Section 5.1. For FRGCv2 dataset, two dense correspondence models are built to cater for the complete data. The first of these models also serves as the gallery for BU3DFE dataset, making this experiment even more challenging. Once the model is morphed and fitted to a query face, we use the resulting parameters  $\alpha$  (7) as features. The Gradient Based Efficient Feature Selection (GEFS) algorithm [63] is used to select the most discriminating features. GEFS is a forward search algorithm

Table 5: Comparison of gender classification results with the state-of-the-art algorithms using 3D features.

Author	Database	# of scans	Male Female	Features Used	Accuracy
Lu et al. [61]	UND	1240	237/139	Range Images	85.4%
Han et al. [64]	GavabDB	427	45/16	Areas/ Volumes	82.6%
Hu et al. [65]	UND	945	205/116	Five facial regions	94.3%
Ballihi et al. [62]	FRGCv2	466	265/201	Radial & circular curves	86.0%
Gilani et al. [60]	FRGCv2	4007	265/201	3D linear & geodesic dist	97.0%
Gilani et al. [59]	BU3DFE	2500	56/44	3D linear & geodesic dist	99.3%
<b>This paper</b>	FRGCv2	4007	265/201	K3DM	99.5%
	BU3DFE	2500	56/44		99.8%

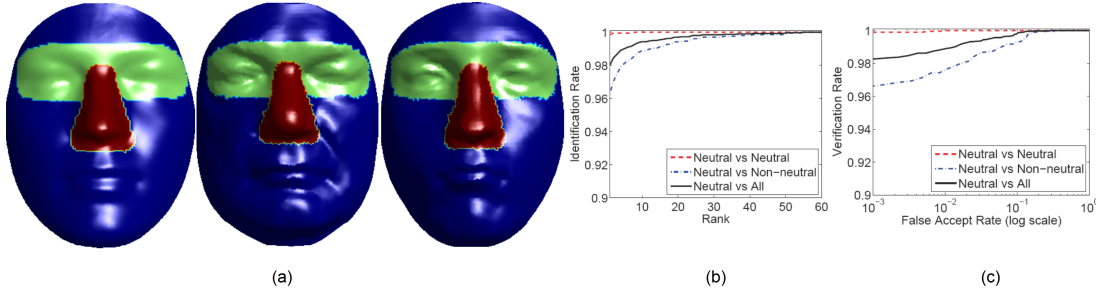


Figure 11: (a) Eyes and nose regions used in face recognition shown on the mean face of K3DM and two identities of FRGCv2. Note that the regions need to be marked on the mean face only. (b) ROC curves for identification and (c) verification tasks on FRGCv2 database using our dense correspondence model and fitting algorithms.

which decides the sequence and number of discriminating features based on the gradient of classification accuracy in each iteration. Finally we train the Linear Discriminant Analysis (LDA) classifier on the selected features to separate the two genders. The gender classification results using our dense correspondence algorithm are given in Table 5 along with a comparison with the state-of-the-art algorithms using 3D features.

### 5.3. Face Recognition

Face is considered as one of the most important biometrics due to its non-intrusive nature. 3D face recognition has addressed many shortcomings of its counterpart in the 2D domain [35]. We consider this application apt to test the quality of the presented algorithms. Note that our main aim is to evaluate our proposed correspondence and model fitting algorithms as opposed to presenting a face recognition system *per se*.

We follow the FRGC protocols of face recognition and include only one scan of each individual (466 in total) in the gallery. To demonstrate the effectiveness of our K3DM Augmentation algorithm, we construct a dense correspondence model on the first available neutral scans of the first 200 identities of FRGCv2 dataset. The constructed model is then augmented with first available neutral scans of the remaining 266 identities of the database using Algorithm 3. The gallery set now contains the first available neutral expression scans of the 466 identities of FRGCv2. The probe set consists of the remaining (3,541) scans of all identities. Note that there is only one scan per identity for 56 individuals

Table 6: Comparison of 3D face recognition results with the state-of-the-art in terms of Rank-1 identification rate (I-Rate) and verification rate (V-Rate) at 0.1% FAR.

Author	Neutral		Non-neutral		All	
	I-Rate	V-Rate	I-Rate	V-Rate	I-Rate	V-Rate
Mian et al.[44]	99.4%	99.9%	92.1%	96.6%	96.1%	98.6%
Kakadiaris et al.[33]	-	99.0%	-	95.6%	97.0%	97.3%
Al-Osaimi et al.[68]	97.6%	98.4%	95.2%	97.8%	96.5%	98.1%
Queirolo et al.[66]	-	99.5%	-	94.8%	98.4%	96.6%
Drira et al.[69]	99.2%	-	96.8%	-	97.7%	97.1%
<b>This paper</b>	99.9%	99.9%	96.3%	96.6%	98.0%	98.3%

in the dataset. All of these identities appear only in the gallery. Furthermore, a quick inspection of the database reveals that two persons have been allotted duplicate identities. Identity number *04637* and *04638* belong to the same person and similarly *04643* and *04783* belong to the same person. The latter has been acknowledged by FRGCv2 dataset providers [66]. Since, both persons have a total of six and five scans only, merging their identities does not effect the face recognition results. In order to report consistent comparisons with the state-of-the-art, we did not correct this error. The complete dataset was further classified into “neutral” and “non-neutral” expression subclasses following the protocol outlined in [44] to evaluate the effects of expressions on deformable model fitting and face recognition.

We employ a holistic and region based approach to model fitting and face recognition. It is well known that the generalization of a model can be increased by dividing faces into independent subregions that are morphed independently [30]. This technique has been used extensively for face recognition [3, 35] and recently for matching off springs to their parents [67]. We also use this approach and perform face recognition by morphing the complete face as well as the eyes and nose regions (see Figure 11(a)). We define these regions on the mean face which is sufficient to transfer the information to all the faces in the dense correspondence model. In the first step the K3DM is morphed and fitted to each query face in the probe as a whole. The presence of expression in the query face results in duplicate correspondences in regions of gaps or discontinuities. Removing the points pertaining to duplicate correspondences in the fitting process mitigates the effects of facial expression.

In the next step, we morph the eyes and the nose regions separately to each query face and obtain model parameters ( $\alpha$ -Step 12 in Algorithm 2) for these regions. Finally, the parameters from the whole face and the regions are concatenated to form the feature vector for face recognition. We then perform feature selection using the GEFS algorithm [59] on the training data set of FRGCv2 containing 953 facial scans. Note that these scans are not used in testing the face recognition algorithm. The selected features of each query face are matched with those of the gallery faces in the model. The query face is assigned the identity of the gallery face with which it has the smallest distance  $d_f = \cos^{-1} \frac{\tilde{\alpha}_M^T \tilde{\alpha}_Q}{\|\tilde{\alpha}_M\|_2 \|\tilde{\alpha}_Q\|_2}$ , where  $\tilde{\alpha}_M$  are the selected features of each face in K3DM and  $\tilde{\alpha}_Q$  are the selected features of the query face.

Figure 12 shows the process of model fitting in PCA space. The dense correspondence model is iteratively fitted on the query face, which in the figure is an extreme expression scan of the first identity. The model fitting starts from the mean face and in each iteration the fitted query model traverses closer to its gallery face in the PCA space. Face recognition is performed when the fitting residual error  $\epsilon_f$  is less than  $10^{-4}$ .

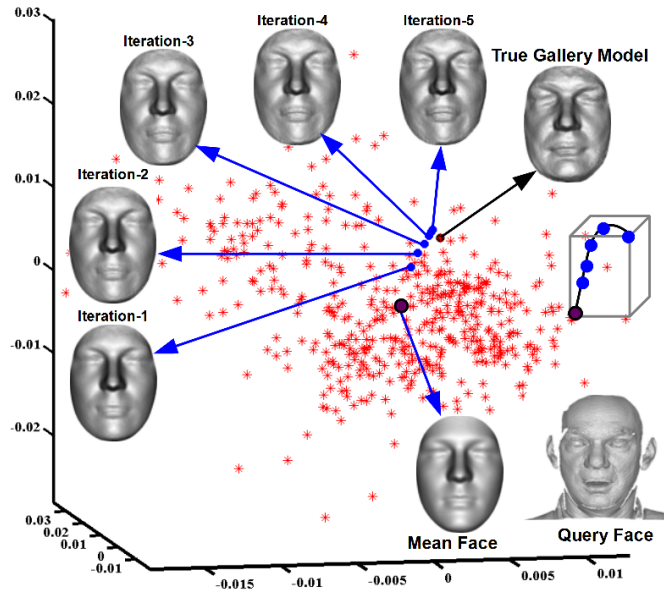


Figure 12: Illustration of iterative model fitting. The 466 FRGCv2 identities are depicted as red stars in the first three PC space. The model is morphed iteratively into the query face until the residual error is negligible. Notice how the fitting process takes the query face through a non-linear path (inset image) and removes the extreme facial expression from the query and generates its equivalent neutral expression model.

Figure 11(b-c) show the CMC and ROC curves of our algorithm. Rank-1 identification rate for neutral probes is 99.85% while 100% accuracy is achieved at Rank-8. In the more difficult scenario of neutral vs non-neutral, the Rank-1 identification rate is 96.3%. A similar trend is observed in the verification rates at 0.1% FAR. Table 6 compares our algorithm with the state-of-the-art. In most cases, our results are better than the state-of-the-art depicting the high quality of the dense correspondence model.

## 6. Conclusion

We have proposed an algorithm that simultaneously establishes dense correspondences between a large number of 3D faces. Based on the dense correspondences, a deformable face model was constructed. We also proposed morphable model fitting and updating algorithms that are useful for landmark identification, face recognition and gender classification. Thorough experiments were performed on synthetic and real 3D faces. Comparison with existing state-of-the-art shows that our algorithm achieves better or comparable performance on all three tasks.

## Acknowledgements

This research is supported by ARC DP110102399 and FECM UWA grants. Syed Zulqarnain Gilani is supported by the International Postgraduate Research Scholarship.

## References

- [1] L. Farkas, Anthropometry of the head and face in clinical practice, Anthropometry of the head and face, 2nd Ed (1994) 71–111.



- [2] P. Nair, A. Cavallaro, 3-d face detection, landmark localization, and registration using a point distribution model, *IEEE Tran. on Multimedia* 11 (4) (2009) 611–623.
- [3] V. Blanz, T. Vetter, Face recognition based on fitting a 3D morphable model, *IEEE TPAMI* 25 (9) (2003) 1063–1074.
- [4] P. Hammond, et al., The use of 3D face shape modelling in dysmorphology, *Archives of disease in childhood* 92 (12) (2007) 1120.
- [5] P. Hammond, C. Forster-Gibson, A. Chudley, et al., Face-brain asymmetry in autism spectrum disorders, *Molecular Psychiatry* 13 (6) (2008) 614–623.
- [6] R. H. Davies, C. J. Twining, T. F. Cootes, J. C. Waterton, C. J. Taylor, 3D statistical shape models using direct optimisation of description length, in: *ECCV*, Springer, 2002.
- [7] R. Davies, C. Twining, C. Taylor, *Statistical models of shape: Optimisation and evaluation*, Springer, 2008.
- [8] T. Heimann, H.-P. Meinzer, Statistical shape models for 3D medical image segmentation: A review, *Medical Image Analysis* 13 (4) (2009) 543–563.
- [9] M. Alexa, Recent advances in mesh morphing, in: *Computer Graphics Forum*, Vol. 21, 2002, pp. 173–198.
- [10] D. Aiger, N. Mitra, D. Cohen, 4-points congruent sets for robust pairwise surface registration, in: *ACM TOG*, Vol. 27, 2008, p. 85.
- [11] B. Brown, S. Rusinkiewicz, Global non-rigid alignment of 3-D scans, in: *ACM TOG*, Vol. 26, 2007, p. 21.
- [12] W. Chang, M. Zwicker, Automatic registration for articulated shapes, in: *Computer Graphics Forum*, Vol. 27, 2008, pp. 1459–1468.
- [13] H. Mirzaalian, G. Hamarneh, T. Lee, A graph-based approach to skin mole matching incorporating template-normalized coordinates, in: *IEEE CVPR*, 2009.
- [14] T. Funkhouser, P. Shilane, Partial matching of 3D shapes with priority-driven search, in: *Eurographics Symposium on Geometry Processing*, Vol. 256, 2006, pp. 131–142.
- [15] G. Passalis, P. Perakis, T. Theoharis, I. A. Kakadiaris, Using facial symmetry to handle pose variations in real-world 3D face recognition, *IEEE TPAMI* 33 (10) (2011) 1938–1951.
- [16] U. Prabhu, J. Heo, M. Savvides, Unconstrained pose-invariant face recognition using 3D generic elastic models, *IEEE TPAMI* 33 (10) (2011) 1952–1961.
- [17] O. Van Kaick, H. Zhang, G. Hamarneh, D. Cohen-Or, A survey on shape correspondence, in: *Computer Graphics Forum*, Vol. 30, 2011, pp. 1681–1707.
- [18] Y. Wang, B. S. Peterson, L. H. Staib, Shape-based 3D surface correspondence using geodesics and local geometry, in: *IEEE CVPR*, 2000.
- [19] Y. Sun, M. A. Abidi, Surface matching by 3D point’s fingerprint, in: *IEEE ICCV*, 2001.
- [20] Y. Sun, J. Paik, A. Koschan, D. Page, M. Abidi, Point fingerprint: a new 3D object representation scheme, *IEEE Tran. on Systems, Man, and Cybernetics, Part B: Cybernetics* 33 (4) (2003) 712–717.
- [21] S. Wang, Y. Wang, M. Jin, X. D. Gu, D. Samaras, Conformal geometry and its applications on 3D shape matching, recognition, and stitching, *IEEE TPAMI* 29 (7) (2007) 1209–1220.
- [22] J. Novatnack, K. Nishino, Scale-dependent/invariant local 3D shape descriptors for fully automatic registration of multiple sets of range images, in: *ECCV*, Springer, 2008.
- [23] A. Salazar, S. Wuhrer, C. Shu, F. Prieto, Fully automatic expression-invariant face correspondence, *Machine Vision and Applications* 25 (4) (2014) 859–879.
- [24] L. Yin, X. Wei, et al., A 3D facial expression database for facial behavior research, in: *Automatic Face and Gesture Recognition*, 2006, pp. 211–216.
- [25] X. Lu, A. K. Jain, Automatic feature extraction for multiview 3D face recognition, in: *Automatic Face and Gesture Recognition*, 2006.
- [26] M. Segundo, L. Silva, P. Bellon, C. C. Queirolo, Automatic face segmentation and facial landmark detection in range images, *IEEE Tran. on Systems, Man, and Cybernetics, Part B: Cybernetics* 40 (5) (2010) 1319–1330.
- [27] P. Phillips, P. Flynn, T. Scruggs, K. Bowyer, et al., Overview of the face recognition grand challenge, in: *IEEE CVPR*, 2005.
- [28] C. Creusot, N. Pears, J. Austin, A machine-learning approach to keypoint detection and landmarking on 3D meshes, *IJCV* 102 (1-3) (2013) 146–179.
- [29] P. Perakis, G. Passalis, T. Theoharis, I. A. Kakadiaris, 3D facial landmark detection under large yaw and expression variations, *IEEE TPAMI* 35 (7) (2013) 1552–1564.
- [30] V. Blanz, T. Vetter, A morphable model for the synthesis of 3d faces, in: *ACM Conference on Computer Graphics and Interactive Techniques*, 1999.
- [31] V. Blanz, K. Scherbaum, H.-P. Seidel, Fitting a morphable model to 3d scans of faces, in: *IEEE ICCV*, 2007.
- [32] G. Passalis, I. Kakadiaris, T. Theoharis, G. Toderici, N. Murtuza, Evaluation of 3d face recognition in the presence of facial expressions: an annotated deformable model approach, in: *IEEE CVPR Workshops*, 2005.
- [33] I. A. Kakadiaris, G. Passalis, G. Toderici, M. Murtuza, Y. Lu, N. Karampatziakis, T. Theoharis, Three-dimensional face recognition in the presence of facial expressions: An annotated deformable model approach, *IEEE TPAMI* 29 (4) (2007) 640–649.
- [34] H. Zhang, A. Sheffer, D. Cohen, et al., Deformation-driven shape correspondence, in: *Computer Graphics Forum*, Vol. 27, 2008, pp. 1431–1439.
- [35] A. Mian, M. Bennamoun, R. Owens, An efficient multimodal 2D-3D hybrid approach to automatic face recognition, *IEEE TPAMI* 29 (11) (2007) 1927–1943.
- [36] R. C. Gonzalez, R. E. Woods, *Digital image processing*, 2nd Edition, SL: Prentice Hall, 2002.
- [37] J. D’Erico, Surface fitting using gridfit, in: *MATLAB Central File Exchange*, 2008.
- [38] B. C. Munsell, A. Temlyakov, M. Styner, S. Wang, Pre-organizing shape instances for landmark-based shape correspondence, *IJCV* 97 (2) (2012) 210–228.

- [39] F. L. Bookstein, Principal warps: Thin-plate splines and the decomposition of deformations, *IEEE TPAMI* 11 (6) (1989) 567–585.
- [40] C. B. Barber, D. P. Dobkin, H. Huhdanpaa, The quickhull algorithm for convex hulls, *ACM Tran. on Mathematical Software* 22 (4) (1996) 469–483.
- [41] A. Mian, M. Bennamoun, R. Owens, On the repeatability and quality of keypoints for local feature-based 3D object retrieval from cluttered scenes, *IJCV* 89 (2-3) (2010) 348–361.
- [42] D. Rueckert, L. Sonoda, C. Hayes, et al., Nonrigid registration using free-form deformations: application to breast mr images, *IEEE Tran. on Medical Imaging* 18 (8) (1999) 712–721.
- [43] D.-J. Kroon, Finite iterative closest point, in: *MATLAB Central File Exchange*, 2009.
- [44] A. Mian, M. Bennamoun, R. Owens, Keypoint detection and local feature matching for textured 3D face recognition, *IJCV* 79 (1) (2008) 1–12.
- [45] Y. Guo, F. Sohel, M. Bennamoun, M. Lu, J. Wan, Rotational projection statistics for 3D local surface description and object recognition, *IJCV* 105 (1) (2013) 63–86.
- [46] K. S. Arun, T. S. Huang, S. D. Blostein, Least-squares fitting of two 3D point sets, *IEEE TPAMI* (5) (1987) 698–700.
- [47] F. Tombari, S. Salti, L. Di Stefano, Unique signatures of histograms for local surface description, in: *ECCV*, Springer, 2010.
- [48] C. S. Chua, R. Jarvis, Point signatures: A new representation for 3D object recognition, *IJCV* 25 (1) (1997) 63–85.
- [49] B. C. Munsell, A. Temlyakov, S. Wang, Fast multiple shape correspondence by pre-organizing shape instances, in: *IEEE CVPR*, 2009, pp. 840–847.
- [50] J. A. Sethian, Evolution, implementation, and application of level set and fast marching methods for advancing fronts, *J. of Computational Physics* 169 (2) (2001) 503–555.
- [51] G. Peyré, The numerical tours of signal processing-advanced computational signal and image processing, *IEEE Computing in Science and Engineering* 13 (4) (2011) 94–97.
- [52] J. L. Bentley, Multidimensional binary search trees used for associative searching, *Communications of the ACM* 18 (9) (1975) 509–517.
- [53] A. Todorov, S. Baron, N. Oosterhof, Evaluating face trustworthiness: a model based approach, *Social Cognitive and Affective Neuroscience* 3 (2) (2008) 119–127.
- [54] N. N. Oosterhof, A. Todorov, The functional basis of face evaluation, *Proceedings of the Nat. Acad. of Sciences* 105 (32) (2008) 11087–11092.
- [55] B. C. Munsell, P. Dalal, S. Wang, Evaluating shape correspondence for statistical shape analysis: A benchmark study, *IEEE TPAMI* 30 (11) (2008) 2023–2039.
- [56] V. Kraevoy, A. Sheffer, Cross-parameterization and compatible remeshing of 3D models, in: *ACM TOG*, Vol. 23, ACM, 2004, pp. 861–869.
- [57] P. Szeptycki, M. Ardabilian, L. Chen, A coarse-to-fine curvature analysis-based rotation invariant 3D face landmarking, in: *Biometrics: Theory, Applications, and Systems*, IEEE, 2009.
- [58] S. Z. Gilani, K. Rooney, F. Shafait, M. Walters, A. Mian, Geometric facial gender scoring: Objectivity of perception, *PloS one* 9 (6).
- [59] S. Z. Gilani, A. Mian, Perceptual differences between men and women: A 3D facial morphometric perspective, in: *IEEE ICPR*, 2014.
- [60] S. Z. Gilani, F. Shafait, A. Mian, Biologically significant facial landmarks: How significant are they for gender classification?, in: *IEEE DICTA*, 2013.
- [61] X. Lu, H. Chen, A. K. Jain, Multimodal facial gender and ethnicity identification, in: *Advances in Biometrics*, Springer, 2005, pp. 554–561.
- [62] L. Ballihi, B. Ben Amor, M. Daoudi, A. Srivastava, D. Aboutajdine, Boosting 3D geometric features for efficient face recognition and gender classification, *IEEE Tran. on Information Forensics and Security* 7 (6) (2012) 1766–1779.
- [63] S. Z. Gilani, F. Shafait, A. Mian, Gradient based efficient feature selection, in: *IEEE WACV*, 2014.
- [64] X. Han, H. Ugail, I. Palmer, Gender classification based on 3d face geometry features using svm, in: *IEEE Int'l Conference on CyberWorlds*, 2009.
- [65] Y. Hu, J. Yan, P. Shi, A fusion-based method for 3d facial gender classification, in: *IEEE ICCAE*, 2010.
- [66] C. Queirolo, L. Silva, O. Bellon, M. Segundo, 3D face recognition using simulated annealing and the surface interpenetration measure, *IEEE TPAMI* 32 (2) (2010) 206–219.
- [67] A. Dehghan, E. Ortiz, R. Villegas, M. Shah, Who do i look like? determining parent-offspring resemblance via gated autoencoders, in: *IEEE CVPR Workshops*, 2014, pp. 171–171.
- [68] F. Al-Osaimi, M. Bennamoun, A. Mian, An expression deformation approach to non-rigid 3D face recognition, *IJCV* 81 (3) (2009) 302–316.
- [69] H. Drira, B. Ben Amor, A. Srivastava, M. Daoudi, R. Slama, 3D face recognition under expressions, occlusions, and pose variations, *IEEE TPAMI* 35 (9) (2013) 2270–2283.